Cross-Beam Energy Transfer: Polarization Effects and Evidence of Saturation
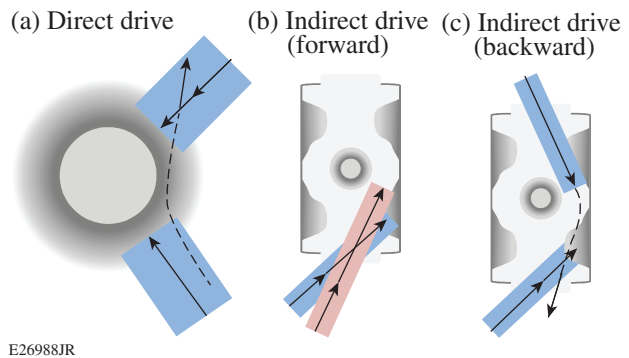
Introduction

Stimulated Brillouin scattering (SBS), one of the most common three-wave laser–plasma instabilities, occurs when an electromagnetic wave "pump" decays into a second frequency-downshifted electromagnetic wave "probe" and an ion-acoustic wave (IAW). The decay is resonant when the following holds:

$$\omega_0 - \omega_1 = (\mathbf{k}_0 - \mathbf{k}_1) \cdot \mathbf{V} + \left| \mathbf{k}_0 - \mathbf{k}_1 \right| c_s, \qquad (1)$$

where ω is the frequency; k is the wave number; the subscripts 0 and 1 refer to the pump and probe, respectively; V is the plasma-flow velocity; and c_s is the sound speed. The use of a stationary plasma ($|\mathbf{V}| = 0$) makes clear that the formula satisfies conservation of both energy [$\hbar\omega_0 = \hbar(\omega_1 + \omega_{IAW})$, where $\omega_{IAW} = k_{IAW}c_s$ is the IAW frequency] and momentum [$\hbar k_0 = \hbar(k_1 + k_{IAW})$]. In the absence of a plasma-flow velocity, a frequency difference between the two electromagnetic waves is required such that the resulting beat frequency matches the finite ion-acoustic wave frequency. Another straightforward limit occurs when the plasma-flow velocity projected along the direction of the beat wave is equal to the sound speed; in this moving frame, the electromagnetic wave frequencies are Doppler shifted such that their beat frequency resonantly drives the finite-frequency IAW in the same manner. A combination of flow velocity and frequency-shifted electromagnetic waves can satisfy this formula in a similar manner.

When the instability grows from the thermal density modulations present in any finite-temperature plasma (i.e., noise), it is typically referred to as SBS, and direct backscatter tends to dominate the overall scattered light because the ponderomotive force driving the IAW density modulation is strongest for oppositely directed electromagnetic waves. When the instability is seeded by an electromagnetic wave with an amplitude much larger than that of the thermal noise, as first described by Randall *et al.*,[1] it has come to be referred to as cross-beam energy transfer (CBET). CBET can result in scattered light at a wider range of angles, dictated by the direction of the electromagnetic seed.

In direct-drive inertial confinement fusion (ICF),[2] targets are typically driven symmetrically with frequency-degenerate laser beams. CBET occurs when rays from the outer edge of a given beam refract through the corona and bypass the target without being absorbed. When these rays overlap other incident beams in a location where the target's exhaust velocity renders frequency-degenerate interactions resonant (close to the Mach-1 surface), energy is transferred from the incoming to the outgoing rays, introducing drive asymmetries as well as reducing the laser ablation pressure and capsule drive [Fig. 153.26(a)]. This has been observed on the basis of scattered-light and implosion-velocity measurements.[3–7]

(a) Direct drive (b) Indirect drive (forward) (c) Indirect drive (backward)

E26988JR

Figure 153.26
Illustrations of ways that cross-beam energy transfer (CBET) can occur in ICF targets, showing just two beams. (a) In direct drive, edge rays from each beam can bypass the target and be amplified by other incident beams in the expanding corona surrounding the capsule. (b) In indirect drive, CBET occurs between incident beams in the laser entrance hole region and is primarily controlled by frequency detuning the lasers. (c) A different type of CBET was recently observed in indirect-drive hohlraums, where it was found that specular reflections could seed CBET in the plasma expanding from the hohlraum wall.

In indirect-drive ICF[8] at the National Ignition Facility (NIF), CBET usually refers to the transfer of energy between the 96 full-energy beams overlapping in each laser entrance hole of a hohlraum target.[9–13] Since the flows in the entrance region are typically much less than the sound speed, CBET

is usually controlled by introducing a frequency difference between different cones of incident beams in order to tailor the distribution of laser intensity within the hohlraum interior [Fig. 153.26(b)]. Recently, however, an additional form of CBET was observed in hohlraums: specular reflections and/or backscatter from one cone of beams was shown to be reamplified by a different set of beams [Fig. 153.26(c)], which complicated the understanding and diagnosis of scattered light from such targets.[14] This latter process resembles the direct-drive version of CBET.

In all cases, a proper accounting of CBET is vital for predictive modeling of ICF implosions. In this article, we will first review the model that is used to calculate CBET in indirect-drive experiments on the NIF along with a recent experiment showing excellent agreement with the theory. We will then present additional data in which the incident probe-beam energy was increased in order to access larger IAW amplitudes, which resulted in deviation from linear theory and evidence of IAW saturation. The data indicate that IAW's are saturated at the $\delta n/n \approx 0.015$ level for the laser and plasma parameters of the experiment. Next, we will review the ability to manipulate a probe beam's polarization using CBET, along with an example showing the complexity that arises from such polarization effects in a multibeam configuration such as those typical in ICF research. Finally, we will present our conclusions.

CBET Linear Theory

In this section, the essential features of the model presented by Michel *et al.* (Ref. 15 and references therein) are summarized. The pump and probe are described by normalized laser vector potentials $\mathbf{a} = e\mathbf{A}/(m_e c^2) \approx 8.55 \times 10^{-10} (I\lambda_{\mu m}^2)^{1/2}$, where I is the laser intensity (W/cm^2) and $\lambda_{\mu m}$ is the laser wavelength in microns. The effect of an electromagnetic pump beam on a probe beam in a plasma can be described by a refractive-index perturbation $\delta\eta$. Interacting with the pump over some length L, a component (specified later) of the probe laser is modified by the operator $\exp(ik_1\delta\eta L/\eta_0)$, where $\eta_0 = \sqrt{1 - n_e/n_c}$ is the unperturbed plasma's refractive index, given electron density n_e and critical density n_c. Using a kinetic model, the refractive-index perturbation is given by

$$\delta\eta = (1/2)K * |\pi_0|^2 \sin(\psi/2)\tan(\psi/2),$$

where $K = \chi_e(1 + \chi_i)/(1 + \chi_e + \chi_i)$; the electron and ion ($\alpha$ = e,i) susceptibilities in thermodynamic equilibrium are $\chi_\alpha = -(1/2)(k_b\lambda_{D_\alpha})^{-2} Z'[v_b/(\sqrt{2} v_{T_\alpha})]$; $\mathbf{k}_b = \mathbf{k}_0 - \mathbf{k}_1$ is the beat wave's wave number; $\lambda_{D_\alpha} = v_{T_\alpha}/\omega_{P_\alpha}$ is the Debye length;

$v_{T_\alpha} = (T_\alpha/m_\alpha)^{1/2}$ is each particle's thermal velocity with T_α and m_α its temperature and mass; $\omega_{P_\alpha} = (4\pi n_\alpha q_\alpha^2/m_\alpha)^{1/2}$ gives the electron and ion plasma frequencies; Z is the plasma dispersion function; $v_b = \omega_b/k_b$ is the beat wave's phase velocity; $\omega_b = \omega_0 - \omega_1$ is the beat wave's frequency; and $|\pi_0|^2 = |\mathbf{a}_{0_p}|^2 \cos^2\psi + |\mathbf{a}_{0_s}|^2$ is the pump amplitude projected into the plane of the probe's polarization, where the p component is in the plane defined by the pump and probe $\mathbf{k}$ vectors and the s component is orthogonal to that plane, and ψ is the crossing angle between the two beams.

The model assumes the following: The interaction has reached steady state, which occurs on ion-acoustic time scales; the spatial variations of the ion-acoustic wave are assumed small compared to the beat wave's wavelength; and the variations of the pump and probe envelopes along the interaction bisector are small compared to the laser wavelength.

It is crucial to note two key features of the model in order to understand polarization effects in CBET as well as the experimental results that will be presented: The first key point is that, for arbitrary polarizations, the interaction is generally anisotropic—only the component of the probe's polarization that is parallel to π_0 is affected by the pump–plasma system (i.e., modified by the operator given above); any orthogonal probe polarization component is unaffected by the system [Fig. 153.27(a)].

The second key point is that $\delta\eta$ is complex. The imaginary component is typically assumed to govern CBET because it modifies the amplitude of the probe beam and peaks at the ion-acoustic resonance, as expected. The fact that there is an associated real component—directly related to the imaginary component by the Kramers–Kronig relations—is true of many systems with frequency-dependent optical resonances (e.g., electric susceptibility, magnetic susceptibility, electrical conductivity, and thermal conductivity) and widely applicable in all areas of physics. A modification of the plasma's real refractive index (only in the direction of the pump polarization) implies that the probe encounters birefringence. Since the real component describes the out-of-phase response of the system, it can be nonzero even for cases in which the imaginary component disappears and CBET may be assumed to be negligible. An example will be provided later to show how this real component could dramatically alter CBET in a multibeam interaction. The solid curves shown in Fig. 153.27(b) are an example of the real and imaginary components calculated with this model for the parameters of an experiment to be discussed in the next section.
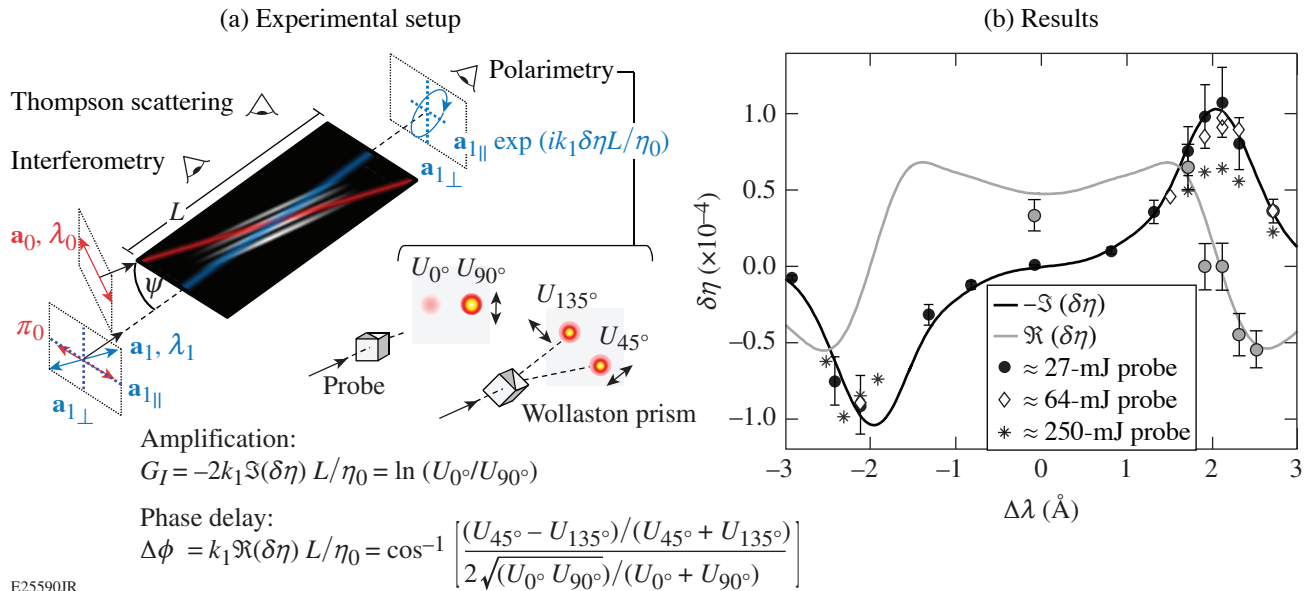
Figure 153.27

Refractive index of a pump–plasma system. (a) An experiment was conducted in which a weak probe beam, with polarization oriented at 45°, interacted with a horizontally polarized pump. Only the probe's horizontal component sees the refractive-index perturbation induced by the pump–plasma system. The probe polarization subsequent to the interaction is used to infer the magnitude of the refractive-index perturbation. (b) Linear theory calculations are plotted with three sets of data points for parameters listed in Table 153.VII. There is good agreement for the weaker injected probe beams, but clear deviation at the highest probe energy, indicating nonlinearity.

Experimental Results

1. Setup

Several experiments were conducted recently at Lawrence Livermore National Laboratory's Jupiter Laser Facility using the Janus laser. Many of the results have been presented in prior publications.[16,17] A long (≈3-ns square), high-intensity pump pulse was focused onto a gas jet equipped with a 3-mm-diam outlet emitting methane gas. A phase plate was used to give the pump beam a flattop but speckled 600-μm-diam focal spot. The pump energy for the shots shown in Fig. 153.27(b) was 292±8 J, giving an expected average intensity of $I = (3.6\pm0.2) \times 10^{13}$ W/cm^2 at the time of the interaction. The peak of an ≈250-ps Gaussian probe beam was timed to arrive ≈1.3 ns after the rising edge of the pump. It was focused using a 200-μm-diam phase plate and crossed the pump at an angle of 27° away from co-propagation.

To measure the refractive index perturbation induced by the pump–plasma system, the pump polarization was horizontal (*p* polarized), whereas the probe polarization was oriented at 45° using a polarizer. This meant there were nearly equal probe polarization components interacting and not interacting with the pump. Separating the probe polarization into constituent components along the *s*- and *p*-polarization directions relative to the two-beam interaction, as well as 45° relative to those

axes, provides a measurement of both the probe amplification (i.e., energy transfer) and any phase delay induced by the real refractive-index component. The polarimetry diagnostic and the formulas for extracting these values from the data are shown in Fig. 153.27(a). For a gain measurement only, it is sufficient to make a single measurement of the *s*- and *p*-polarization components. Conversely, for pure phase delays and no energy transfer (in the case of frequency-degenerate beams), it is sufficient to make a single measurement along the axes rotated 45°.

Both beams used the first harmonic of an Nd:YLF laser source ($\lambda \approx 1053$ nm), but independent front ends allowed us to measure CBET as a function of wavelength detuning between the two beams (here, a range of $-3 \leq \Delta\lambda \leq 3$ Å was used).

Plasma density and electron temperature were measured with Thomson scattering and interferometry. The Thomson-scattering diagnostic collected scattered light from the pump beam in a 90° (vertical) geometry relative to the pump propagation. The blue-shifted electron plasma wave feature was recorded on a streak camera with an S1 photocathode, set to a 5-ns sweep speed. An example of the data is shown in Fig. 153.28(a). Since a high-density, low-Mach-number nozzle was used in conjunction with the large-diameter pump beam,

the diagnostic collected light from a volume spanning $600~\mu$m in the vertical direction, encompassing a wide range of densities. It was necessary to include a range of electron densities spanning $\approx(1$ to $1.4) \times 10^{19}$ cm^{-3} to fit the Thomson data at the time of interaction [shown as the dashed line in Fig. 153.28(a) relative to the Thomson data as well as the pump pulse shape as recorded on a fast diode and oscilloscope] on each shot.

The interferometry data, which used an ultrashort Ti:sapphire beam incident on the channel perpendicular to the pump beam and imaged onto a charge-coupled–device camera using a Nomarski configuration, further constrained the density throughout the interaction. An example of the chord-integrated density–length product is shown in Fig. 153.28(b). It showed that the highest densities in the Thomson volume were actually below the center of the two-beam interaction (≈1.5 mm above the nozzle, which is visible at $y = 0$ mm in the image). Further-

more, the density decreased on either side along the ≈1.2-mm interaction length such that the path-integrated density was $\approx88\%$ of the peak density measured by Thomson scattering. These considerations were factored into the parameters listed in the Table 153.VII.

Table 153.VII: Plasma parameters.

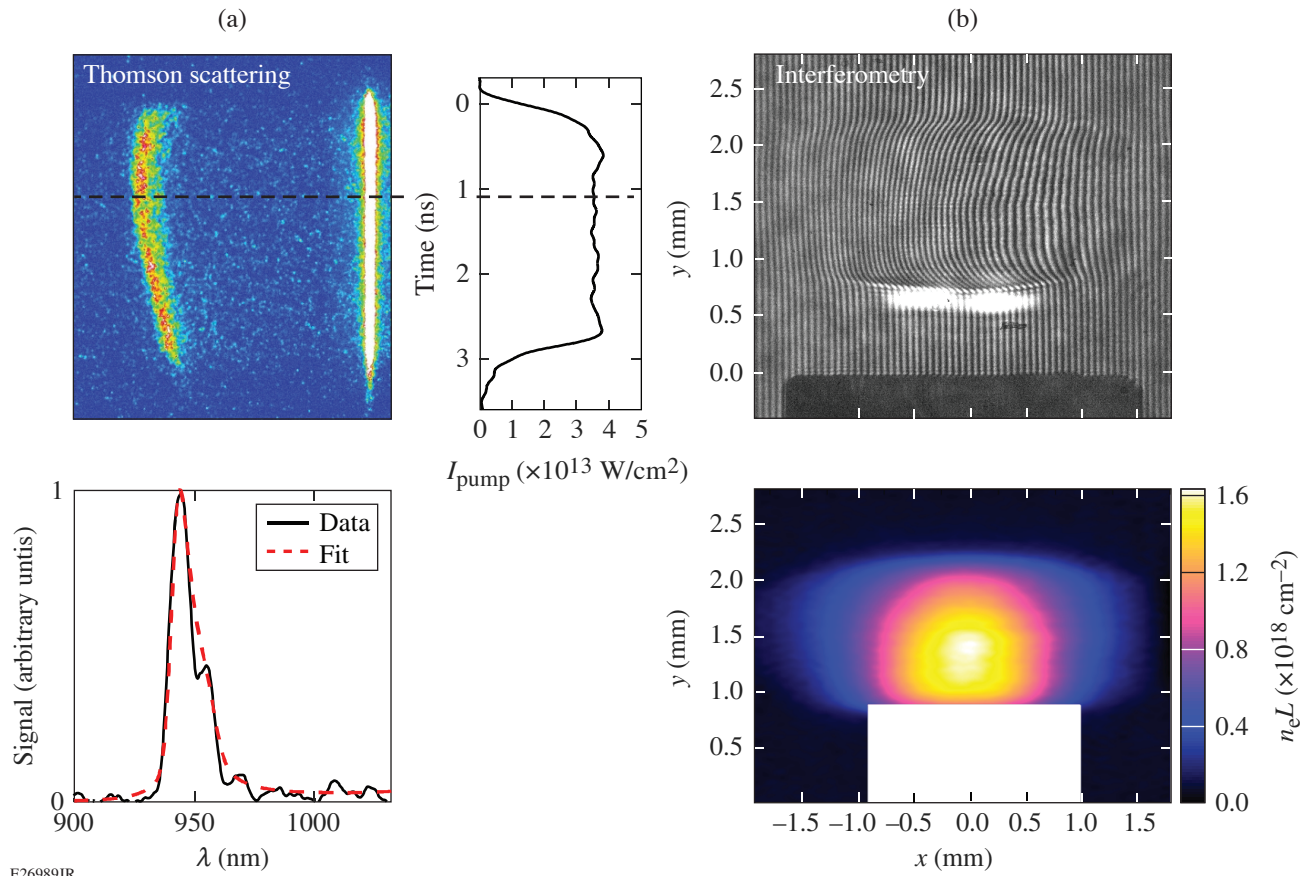| Parameter	Theory input	Measured value	*HYDRA* simulation
n_e/n_c	0.0104	0.11±0.001	0.009
T_e (eV)	220	224±4	$\approx$231
T_i/T_e	0.115	–	$\approx$0.09
V_{flow} (m/s)	1.4×10^4	–	$\approx1.4 \times 10^4$
I_0 (W/cm^2)	$\approx3.2 \times 10^{13}$	$\approx(3.6\pm0.2) \times 10^{13}$	$\approx3.6 \times 10^{13}$
$\overline{Z}$	2.5	–	2.0

(a)

(b)

E26989JR

Figure 153.28
Diagnostics for density and electron temperature. (a) The blue-shifted electron feature was collected at 90° and recorded on an S1 streak camera using a 5-ns sweep. It was analyzed at the time of the probe interaction, shown as a dashed line relative to the pump pulse shape, recorded on a fast diode/oscilloscope. (b) A Nomarski interferometer used an ultrashort Ti:sapphire diagnostic beam—incident perpendicular to the channel and co-timed with the probe—to measure density gradients in the Thomson volume and along the length of the pump–probe interaction.

While this platform aimed to isolate CBET from hydrodynamic uncertainties, nevertheless a flow velocity resulted from the cylindrical plasma channel expansion following formation by the pump beam. Varying the interferometry beam timing relative to channel formation clearly showed this expansion; it is also the reason why the channels were so much larger than the pump beam's diameter at the time of the interaction [Fig. 153.28(b)]. By Doppler shifting the ion-acoustic wave by different amounts in different portions of the crossing volume, this flow effectively broadened the resonant peak. Flow velocity and ion temperature (not measured) were imported to the linear theory calculation from a 3-D simulation of the experiment using the radiation–hydrodynamic code *HYDRA*.[18]

2. Results

Experimental results for three different data sets were shown in Fig. 153.27(b). The most-extensive data set (already published in Ref. 17) used an incident probe beam with 27 mJ of energy. For that data set, several shots were repeated with the Wollaston prism in the polarimetry diagnostic rotated 45° to measure the real refractive index perturbation component in addition to the amplification. Agreement with linear theory was found to be excellent for both the real and imaginary components.

While most of the parameters used in the linear theory calculation were consistent with experimental measurements and the *HYDRA* simulation, the average ion charge state was an exception. To match the resonant peak location, the plasma was assumed to consist of 30% carbon, rather than the 20%, which might be expected when using methane gas. In Ref. 17, it was conjectured that this might have resulted from ion species separation in the expanding plasma channel. Recent efforts to confirm this experimentally, using simultaneous ion and electron feature Thomson scattering and a gas-jet mixture of hydrogen and argon, failed to observe the predicted effect. It is perhaps more likely that the discrepancy arises from a simple error in measuring the two laser wavelengths. When measured, they were found to differ from the nominal laser wavelengths; a correction was applied, but this correction shifted the experimental data away from the linear theory. Better agreement would be obtained by assuming that the correction should have been made in the opposite direction. Figure 153.27(b), however, retains the possibly incorrect wavelength axis for the data and the slightly higher carbon concentration. Note also that accounting for a factor of $\cos(\psi)$ that was missing in the calculations of Ref. 17 better reconciles the pump intensity used in the linear theory calculation here with that expected from measurements, as shown in Table 153.VII.
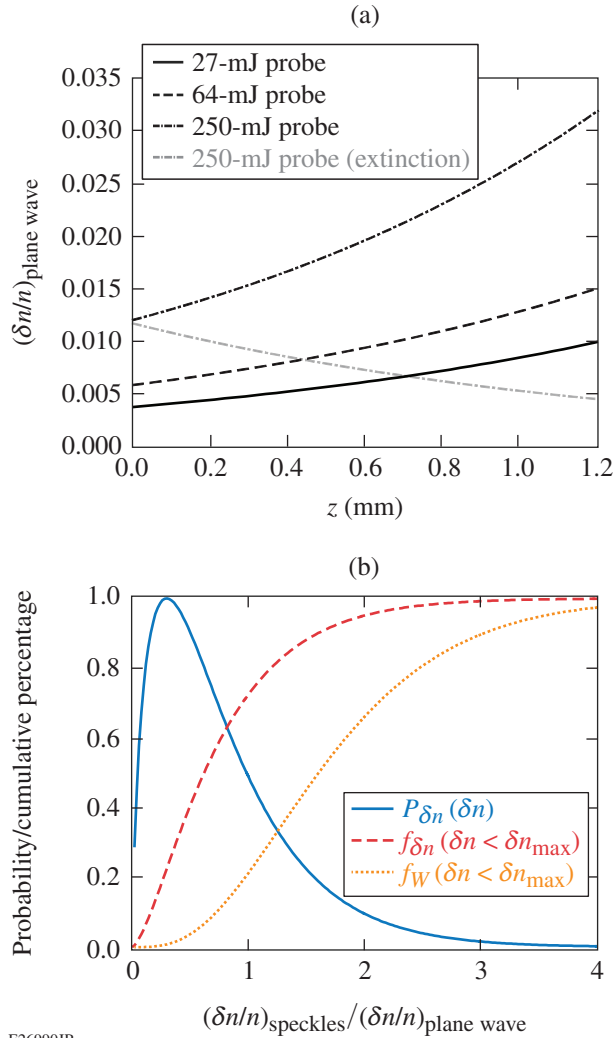
Here we present additional amplification data in which the incident probe energy was increased to ≈ 64 mJ and ≈ 250 mJ. These additional data sets lack error bars for simplicity, but they are comparable to those on the low-energy imaginary component data. The average incident probe intensities were $I \approx (3.4, 8.1, 32) \times 10^{11}$ W/cm^2, approximately half of which gets amplified by CBET because of the 45° probe polarization. The fact that the data points deviate from the linear theory calculation, especially on the positive wavelength shift side of the wavelength tuning curve, is a clear indication of nonlinearity.

3. Discussion

The most-straightforward explanation for nonlinearity is pump depletion, where the energy transfer significantly impacts the pump amplitude and leads to reduced gain. The maximum gain for the highest energy data, however, was $G_I = 1.27$ such that the output average probe intensity was $I = 1/2\, I_{\text{init}} \exp(1.27) \approx 5.3 \times 10^{12}$ W/cm^2, which is only $\approx 16\%$ of the pump intensity. Therefore, pump depletion cannot explain the much-reduced gain.

Saturation of ion-acoustic wave amplitudes could also explain the deviation from linearity as well as the fact that it is more prominent for positive wavelength shifts. Figure 153.29(a) shows the expected average IAW amplitude, $\delta n/n = -(1/2)\, K k_{\text{b}}^2 c^2 \omega_{\text{pe}}^{-2} \mathbf{a}_0 \cdot \mathbf{a}_1^*$, as a function of distance interacting with the pump beam when the probe was red shifted to the point of maximum gain for each of the three incident probe energies. In the limit of negligible pump depletion, the IAW amplitude is linear with $\mathbf{a}_1$ such that the amplifying seed drives larger waves. In the case of a 27-mJ injected probe beam, the average IAW amplitude is expected to have been ≈ 0.004 at the beginning of the interaction region, growing to ≈ 0.01 by the end of the interaction region. For a 250-mJ incident probe, IAW amplitudes would be expected to span ≈ 0.012 to 0.032 if the linear theory remained valid. The deviation from linear theory suggests, however, that these larger amplitudes were not accessed. An additional curve is shown for the equivalent trajectory on the opposite side of the wavelength-tuning curve (maximum probe extinction). In this case, IAW amplitudes get smaller with the probe intensity; therefore, nonlinearity is expected to be much less evident.

The effect of speckles must also be taken into account. As discussed in Ref. 19, the intensity distribution present in any speckled beam results in a distribution of beat-wave amplitudes between two speckled beams. The probability function for the local intensity of a speckled laser beam is $P(u) = e^{-u}$ (Ref. 20), where $u = I/\langle I \rangle$ is the local intensity divided by the average.

Figure 153.29

Expected ion-acoustic wave (IAW) amplitudes. (a) Average IAW amplitudes were calculated for each of the data sets shown in Fig. 153.27(b), if linear theory remained valid. They increased over the probe propagation length if the probe was amplified and decreased if the probe was extinguished. (b) The use of speckled beams creates a distribution of IAW amplitudes, and most of the energy transfer is mediated by IAW's that are larger than the expected plane-wave value; consequently, IAW saturation will impact CBET between speckled beams at lower average intensities than CBET between plane-wave beams.

The local energy exchange between two beams is proportional to the intensity product $\Delta W \propto I_0 I_1$. If correlations between the speckle patterns of the two beams can be neglected over the length of the CBET interaction region, the probability distribution for energy exchange is given by the product distribution for the random variables I_0 and I_1,

$$P_W(\Delta W) = \int_0^\infty P(u_1) P(\Delta W / u_1) \frac{1}{u_1} \, du_1 = 2K_0\left(2\sqrt{\Delta W}\right),$$

where $K_\nu(x)$ is the modified Bessel function of the second kind of order ν. Similarly, the density perturbation is proportional to the square root of the intensity product $\delta n \propto \sqrt{I_0 I_1}$. Since a single beam's probability distribution for the square root of intensity is $P_{sr}(u) = 2u e^{-u^2}$, that of the product is

$$P_{\delta n}(\delta n) = 4 \int_0^\infty \frac{\delta n}{u} e^{-\left(u^2 + \delta n^2 / u^2\right)} du = 4\delta n K_0(2\delta n).$$

Here, the plasma wave amplitude is effectively normalized to the amplitude that would be expected for plane waves having the same average intensity, $\delta n = (\delta n/n)_{\text{speckle}} / (\delta n/n)_{\text{plane wave}}$. The fraction of laser energy exchanged in regions where the local exchange is less than some ΔW_{max} is

$$f_W(\Delta W_{\text{max}}) = \frac{\langle \Delta W \rangle_{\Delta W < \Delta W_{\text{max}}}}{\langle \Delta W \rangle}$$

$$= \frac{\int_0^{\Delta W_{\text{max}}} \Delta W P_W(\Delta W) d\Delta W}{\int_0^\infty \Delta W P_W(\Delta W) d\Delta W}$$

$$= 1 - 2\Delta W_{\text{max}} K_0\left(2\sqrt{\Delta W_{\text{max}}}\right)$$

$$- 2\sqrt{\Delta W_{\text{max}}} \left(1 + \Delta W_{\text{max}}\right) K_1\left(2\sqrt{\Delta W_{\text{max}}}\right). \quad (2)$$

The fraction of laser energy can also be written in terms of the maximum density perturbation because $\sqrt{\Delta W_{\text{max}}} \propto \delta n_{\text{max}}$:

$$f_W(\delta n_{\text{max}}) = 1 - 2\delta n_{\text{max}}^2 K_0(2\delta n_{\text{max}})$$

$$- 2\delta n_{\text{max}}\left(1 + \delta n_{\text{max}}^2\right) K_1(2\delta n_{\text{max}}). \quad (3)$$

The results of this analysis are plotted in Fig. 153.29(b). The probability distribution of the IAW amplitudes (normalized to the amplitude of the plane-wave case) is shown along with its cumulative sum. This shows that, e.g., ≈70% of the IAW's have an amplitude less than the average plane-wave case, whereas ≈30% have an amplitude larger than the plane-wave case and ≈5% of the IAW's are more than a factor of 2 larger than the plane-wave case. The cumulative fraction of energy transferred by IAW's less than a certain amplitude is also shown, making it clear that a disproportionate amount of energy transfer occurs in the relatively small number of intense interactions (e.g., >30% of the energy is tranferred by IAW's with amplitudes at least 2× larger than the expected plane-wave value). Therefore, nonlinearity will impact speckled beams earlier

than plane-wave beams when IAW amplitudes are near the saturation threshold.

Examining the data shown in Fig. 153.26(b) more closely, along with the trajectories shown in Fig. 153.29(a), suggests that IAW amplitudes may be clamped at the $\delta n/n \approx 1\%$ to 2% level. The modest reduction in gain at the IAW resonance peak for the 64-mJ injected probe could be explained by saturation in IAW's driven by the highest-intensity speckles late in the interaction. Furthermore, even average-amplitude IAW's were expected to exceed such a level for the 250-mJ data; therefore, the clamp would impact that data more severely.

To confirm this analysis, CBET simulations were performed using the numerical code *VAMPIRE*.[21] *VAMPIRE* is a fully 3-D propagation model that solves the coupled-mode equations for CBET in steady state, using linear kinetic theory for the IAW response. Laser-intensity distributions in plasma are computed from the position of stochastically distributed geometrical optics rays using a modified tesselation-based estimator. The model reproduces intensity distributions of phase-plate–smoothed beams down to speckle radii of approximately twice the real speckle radius. It also accounts for laser refraction, the finite f number of interacting beams, inverse Bremsstrahlung absorption, and CBET per polarization component (although the real refractive index component is neglected). The negligible effect of pump depletion was confirmed by observing no significant difference between simulations that did or did not include pump depletion.

Results from simulations that clamped IAW amplitudes at $\delta n/n = 1.5\%$ are compared to the data in Fig. 153.30. Note that the wavelength axis for the data has been shifted to account for the possible errors discussed above, which facilitates a comparison of the peak gain in both data and simulations. The simulations matched all of the data quite well, with the clamp having no effect for the lowest-energy incident probe, a marginal effect for the mid-level case, and a dramatic effect on the highest-energy incident beam, especially on the positive wavelength shift side (probe amplification), as expected. The fact that such a large amount of data, with fairly different conditions in each case, was fit very well with a single clamp makes a compelling case that the clamp is a realistic way of accounting for the IAW saturation.

Previous attempts to explain IAW saturation have invoked frequency detuning because of kinetic nonlinear frequency shifts associated with trapped ions,[10,22] increased Landau damping and/or frequency detuning cause by ion heating,[23,24] nonlinear damping associated with mode coupling to higher har-
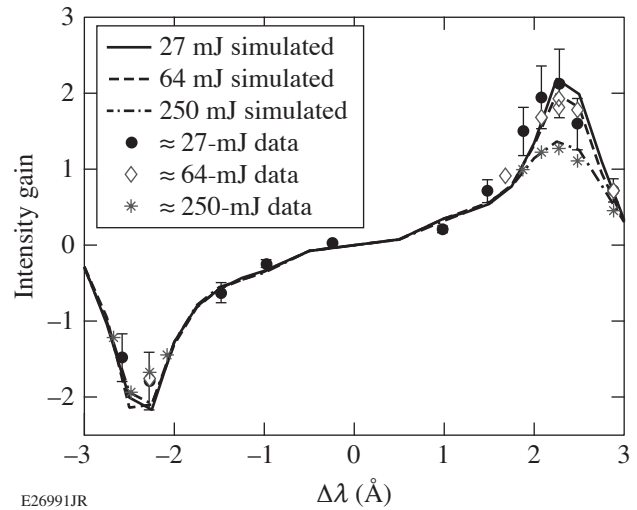

Figure 153.30
The experimental data were compared to simulations using *VAMPIRE*. Including an IAW clamp of $\delta n/n = 1.5\%$ yielded good agreement with all data sets, suggesting IAW's were saturated at that level.

monics,[25–27] and the two-ion-wave decay instability.[28–30] The possible influence of these effects will be considered in turn.

Frequency detuning from a kinetic nonlinear frequency shift does not seem to be a plausible explanation for the saturation observed in this experiment. The magnitude of the expected shift for the IAW amplitudes in question is expected to be quite small, especially when including the contribution of trapped electrons as well as trapped ions.[31] The expected frequency shifts are unlikely to compete with the broad resonance observed in this experiment because of the ion Landau damping provided by hydrogen ions.[32]

Similarly, the already high ion Landau damping makes the interaction relatively insensitive to ion temperature such that ion heating should not substantially alter the gain. Also, if ion heating caused a shift in the resonance peak location, it would have resulted in higher gain at larger frequency shifts between the pump and probe, which was not observed.

The body of work on nonlinear damping associated with mode coupling is primarily concerned with understanding the interplay between various instabilities. If another instability drives a different IAW in the same volume of plasma, it could interfere with the primary wave mediating CBET. However, this two-beam configuration limits the number of plasma waves that are driven in the plasma, and to our knowledge no other plasma waves should be present. The pump remains the most energetic and intense beam in the plasma, so there is no

reason additional instabilities should be driven by increasing the seed energy, unless they arise from decay of the primary IAW associated with CBET.

Historically, the low apparent threshold for ion-wave saturation observed in this experiment would have ruled out the two-ion-wave decay instability according to fluid theory, which says that the threshold should be proportional to the daughter waves' damping rates, $\delta n / n_{\text{thr}} > 4\left(\nu_{\text{IAW},1} \nu_{\text{IAW},2} \big/ \omega_{\text{IAW},0}^2\right)^{1/2}$ (Ref. 30). It was recently noted, however, that ions trapped by the primary wave can reduce the linear Landau damping rate for both the primary wave and the daughter waves since they have similar phase velocities.[33] In that work, Chapman $et\ al.$ found, using $2D + 2V$ Vlasov simulations, that the two-ion-wave decay threshold was exceeded for IAW amplitudes of $\delta n/n_{\text{thr}} = 0.011$ for a set of parameters for which previous estimates would have suggested a threshold of $\delta n/n_{\text{thr}} = 0.04$ to 0.09. The authors also discussed a similar decay instability that they referred to as the "off-axis instability," which was accessible because of the multi-dimensional nature of the simulation. No threshold was identified

for this transverse instability. These instabilities could plausibly explain the IAW saturation that we observed in the experiment.

Earlier work by Kirkwood $et\ al.$ also employed frequency detuning in a quasi-stationary plasma to measure CBET.[34] Although it was noted that gain stayed constant with increasing probe intensities, suggesting that IAW's remained linear up to an amplitude of $\approx 1\%$, a seemingly conflicting statement was made that the linear gain calculation was off by $20\times$. Recently, this work was revisited and the results appeared to be much more consistent with linear theory.[35] More-recent efforts to use CBET to generate a high fluence beam reached similar conclusions as to the linearity of low-amplitude IAW's.[36]

Polarization Effects

As outlined in Ref. 15 and demonstrated in Refs. 16 and 17, CBET is very sensitive to the polarization of the interacting beams and can, in turn, strongly modify each beam's polarization. The data for the 27-mJ probe amplification at the positive and negative ion-acoustic resonance peaks are shown in Fig. 153.31(a). When
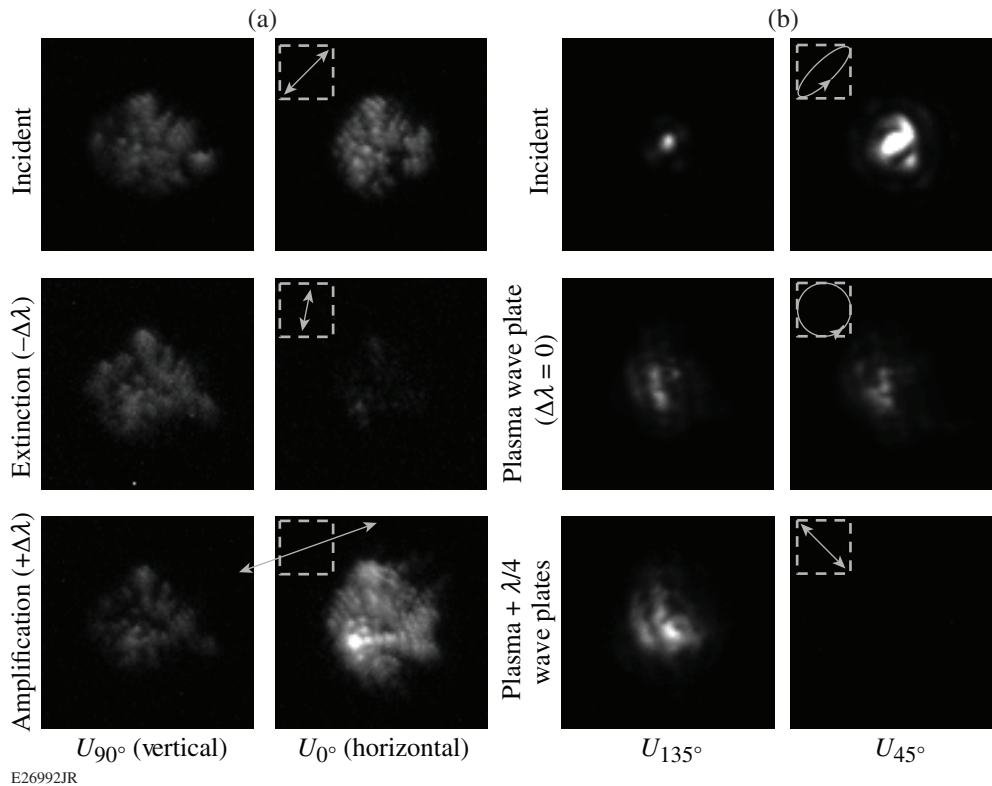

Figure 153.31
Polarization manipulation caused by CBET. (a) Resonant energy transfer at the negative (positive) peak of the ion-acoustic wave extinguished (amplified) the probe and made the probe polarization more orthogonal (parallel) to the pump polarization. (b) Nonresonant interactions were used to convert an elliptically polarized incident probe into a nearly ideal circularly polarized beam without any energy transfer, which was verified by using an additional quarter-wave plate to restore a linear polarization.

the probe is blue shifted relative to the pump, its horizontal polarization is extinguished such that the pump–plasma system acts like a polarizer that passes only the vertical polarization (middle row).[17] This effectively "rotates" the probe polarization, which becomes more orthogonal to the pump as the extinction increases. Conversely, the probe rotates into alignment with the pump when it is red shifted and amplified (bottom row).

Data from a different experiment are reproduced in Fig. 153.31(b). While the setup of that experiment was very similar, one difference was that no phase plate was used in focusing the probe (which is evident in the different focal-spot distribution). The pump and plasma parameters were also different, as well as the incident probe polarization, which was elliptical with a phase delay of $\approx 38°$ between the horizontal and vertical components. Wavelength tuning was not employed in that experiment, but the pump intensity and plasma density were adjusted to control the birefringence resulting from the nonzero real refractive-index modulation. After tuning the pump–plasma system to add a phase delay of $\approx 52°$, the probe became nearly ideally circularly polarized (middle row). The fact that the probe was circular (rather than unpolarized, e.g.) was confirmed by repeating the shot with an additional quartz quarter-wave plate in the diagnostic to add another $90°$ phase delay and recover a linear polarization (bottom row).[16]

These examples illustrate how a pump–plasma system can be used to give a probe beam any arbitrary polarization through amplitude and/or phase changes. Such polarization effects can become particularly complex when considering an environment containing multiple beams in which each beam serves as both pump and probe relative to all other beams present. An example is provided in Fig. 153.32, where each subfigure has curves showing the total normalized vector potential, as well as the s and p components, for each of the three beams. In this calculation, up to three beams intersect in the same plane such that the crossing angle is $27°$ between Beamlines 1 and 2 as well as Beamlines 2 and 3, but $54°$ between Beamlines 1 and 3. Relative to the intersection plane, Beamline 1 is s polarized, Beamline 2 is p polarized, and Beamline 3 is $10°$ away from becoming p polarized. Beamline 1 has a wavelength of $\lambda = 1053$ nm, whereas $\lambda = 1053.285$ nm for Beamlines 2 and 3. All three beam intensities are $I = 5 \times 10^{13}$ W/cm^2, and they interact over a distance of 4 mm in a fully ionized helium plasma with $n_e = 5 \times 10^{19}$ cm^{-3}, $T_e = 200$ eV, and $T_i/T_e = 0.1$.

Figure 153.32(a) shows that nothing happens when only Beamlines 1 and 2 are present because their polarizations are orthogonal. Figure 153.32(b) shows a similar case in which only

Beamlines 2 and 3 are present. Although their polarizations are nearly aligned, their frequencies are also the same, so there is no energy transfer. They do, however, induce ellipticity in one another as a result of the nonzero real refractive index modulation and their slightly misaligned polarizations. These first two cases describe situations in which the two beams would typically be considered "noninteracting."

Figure 153.32(c) shows that when Beamlines 1 and 3 are present, there is polarization rotation resulting from induced phase delay as well as energy transfer caused by the imaginary component of the refractive-index perturbation. Essentially, the beams transfer energy until they reach a state in which the remaining polarizations are orthogonal. The fact that Beamline 3 (1) is amplified (extinguished) is only modestly due to the fact that the polarizations are nearly orthogonal at the outset.

Now consider the case when all three beams are present [Fig. 153.32(d)]. Initially, only a small fraction of Beamline 1 is transferred to Beamline 3 as in case (c), but by inducing a phase
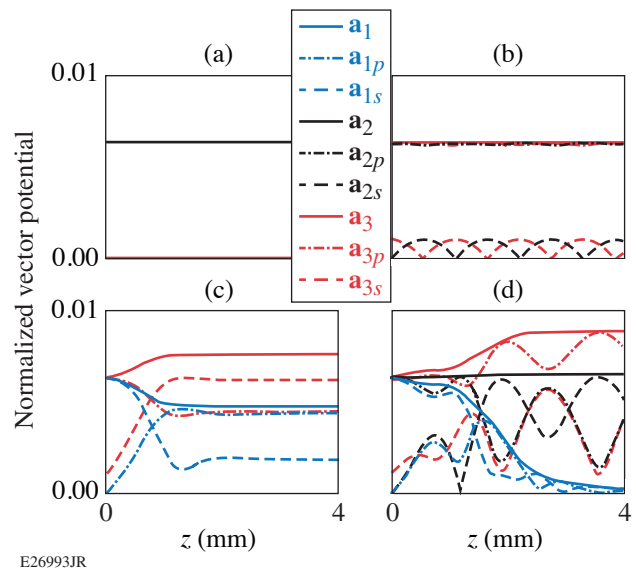

E26993JR

Figure 153.32
CBET between up to three beams for beam/plasma parameters listed in the text. (a) Beamlines 1 and 2 alone see no interaction due to their orthogonal polarizations. (b) Beamlines 2 and 3 alone induce ellipticity in one another but no energy transfer because they are off-resonant (frequency degenerate). (c) Beamlines 1 and 3 alone exchange a modest amount of energy because they have different frequencies and a small shared polarization component, but energy transfer saturates when the polarizations become orthogonal. (d) When all three beams interact, there is a much more dramatic reduction of Beamline 1 and associated amplification of Beamline 3, which results from Beamline 2 acting as a mediator that rotates the Beamline 1 polarization and thereby funnels more energy into a resonant interaction with Beamline 3.

delay in Beamline 1, Beamline 2 acts as a mediator that funnels more energy into a resonant interaction with Beamline 3. This leads to a much more dramatic extinction of Beamline 1 and associated amplification of Beamline 3; all the while the amplitude of Beamline 2 remains approximately constant. This illustrates that polarization effects can have a dramatic influence on CBET in a multibeam configuration, and that even off-resonant interactions can have a large impact on resonant energy transfer.

Conclusions

Various forms of cross-beam energy transfer occur in both direct- and indirect-drive ICF, so a proper accounting of CBET is necessary to accurately model ICF implosions. Recent pump–probe experiments in a quasi-stationary plasma using wavelength tuning to control CBET have been performed to validate the linear theory calculations that are used. These experiments have shown that linear theory appears to be valid for an isolated two-beam interaction with IAW amplitudes up to $\delta n/n \approx 1.5\%$ (which are larger than those expected in ICF experiments[23]), but IAW saturation seems to occur beyond this level. The saturation appears to be consistent with recent work using $2D + 2V$ Vlasov simulations to investigate the two-ion-wave decay instability.[33] Polarization effects of CBET were also reviewed in detail, and it was shown that polarization can have surprising consequences in a multibeam configuration.

REFERENCES

1. C. J. Randall, J. R. Albritton, and J. J. Thomson, Phys. Fluids **24**, 1474 (1981).

2. R. S. Craxton, K. S. Anderson, T. R. Boehly, V. N. Goncharov, D. R. Harding, J. P. Knauer, R. L. McCrory, P. W. McKenty, D. D. Meyerhofer, J. F. Myatt, A. J. Schmitt, J. D. Sethian, R. W. Short, S. Skupsky, W. Theobald, W. L. Kruer, K. Tanaka, R. Betti, T. J. B. Collins, J. A. Delettrez, S. X. Hu, J. A. Marozas, A. V. Maximov, D. T. Michel, P. B. Radha, S. P. Regan, T. C. Sangster, W. Seka, A. A. Solodov, J. M. Soures, C. Stoeckl, and J. D. Zuegel, Phys. Plasmas **22**, 110501 (2015).

3. W. Seka, D. H. Edgell, J. P. Knauer, J. F. Myatt, A. V. Maximov, R. W. Short, T. C. Sangster, C. Stoeckl, R. E. Bahr, R. S. Craxton, J. A. Delettrez, V. N. Goncharov, I. V. Igumenshchev, and D. Shvarts, Phys. Plasmas **15**, 056312 (2008).

4. I. V. Igumenshchev, D. H. Edgell, V. N. Goncharov, J. A. Delettrez, A. V. Maximov, J. F. Myatt, W. Seka, A. Shvydky, S. Skupsky, and C. Stoeckl, Phys. Plasmas **17**, 122708 (2010).

5. I. V. Igumenshchev, W. Seka, D. H. Edgell, D. T. Michel, D. H. Froula, V. N. Goncharov, R. S. Craxton, L. Divol, R. Epstein, R. Follett, J. H. Kelly, T. Z. Kosc, A. V. Maximov, R. L. McCrory, D. D. Meyerhofer, P. Michel, J. F. Myatt, T. C. Sangster, A. Shvydky, S. Skupsky, and C. Stoeckl, Phys. Plasmas **19**, 056314 (2012).

6. A. K. Davis, D. Cao, D. T. Michel, M. Hohenberger, D. H. Edgell, R. Epstein, V. N. Goncharov, S. X. Hu, I. V. Igumenshchev, J. A. Marozas, A. V. Maximov, J. F. Myatt, P. B. Radha, S. P. Regan, T. C. Sangster, and D. H. Froula, Phys. Plasmas **23**, 056306 (2016).

7. D. H. Edgell, R. K. Follett, I. V. Igumenshchev, J. F. Myatt, J. G. Shaw, and D. H. Froula, Phys. Plasmas **24**, 062706 (2017).

8. J. D. Lindl, Phys. Plasmas **2**, 3933 (1995).

9. W. L. Kruer *et al.*, Phys. Plasmas **3**, 382 (1996).

10. E. A. Williams, B. I. Cohen, L. Divol, M. R. Dorr, J. A. Hittinger, D. E. Hinkel, A. B. Langdon, R. K. Kirkwood, D. H. Froula, and S. H. Glenzer, Phys. Plasmas **11**, 231 (2004).

11. P. Michel *et al.*, Phys. Rev. Lett. **102**, 025004 (2009).

12. S. H. Glenzer *et al.*, Science **327**, 1228 (2010).

13. J. D. Moody *et al.*, Nat. Phys. **8**, 344 (2012).

14. D. Turnbull, P. Michel, J. E. Ralph, L. Divol, J. S. Ross, L. F. Berzak Hopkins, A. L. Kritcher, D. E. Hinkel, and J. D. Moody, Phys. Rev. Lett. **114**, 125001 (2015).

15. P. Michel, L. Divol, D. Turnbull, and J. D Moody, Phys. Rev. Lett. **113**, 205001 (2014).

16. D. Turnbull, P. Michel, T. Chapman, E. Tubman, B. B Pollock, C. Y Chen, C. Goyon, J. S Ross, L. Divol, N. Woolsey, and J. D Moody, Phys. Rev. Lett. **116**, 205001 (2016).

17. D. Turnbull, C. Goyon, G. E. Kemp, B. B. Pollock, D. Mariscal, L. Divol, J. S. Ross, S. Patankar, J. D. Moody, and P. Michel, Phys. Rev. Lett. **118**, 015001 (2017).

18. M. M. Marinak *et al.*, Phys. Plasmas **8**, 2275 (2001).

19. R. K. Follett, D. H. Edgell, D. H. Froula, V. N. Goncharov, I. V. Igumenshchev, J. G. Shaw, and J. F. Myatt, Phys. Plasma **24**, 103128 (2017).

20. H. A. Rose and D. F. DuBois, Phys. Fluids B **5**, 590 (1993).

21. A. Colaïtis, T. Chapman, D. Strozzi, L. Divol, and P. Michel, "A Tesselation-Based Model for Intensity Estimation and Laser–Plasma

Interaction Calculations in Three Dimensions," to be published in Physics of Plasmas.

22. B. I. Cohen *et al.*, Phys. Plasmas **5**, 3408 (1998).

23. P. Michel *et al.*, Phys. Rev. Lett. **109**, 195004 (2012).

24. P. Michel *et al.*, Phys. Plasmas **20**, 056308 (2013).

25. K. Estabrook, W. L. Kruer, and M. G. Haines, Phys. Fluids B **1**, 1282 (1989).

26. W. L. Kruer *et al.*, Phys. Scr. **1998**, T75 (1998).

27. C. Labaune *et al.*, Phys. Rev. Lett. **82**, 3613 (1999).

28. C. Niemann, S. H. Glenzer, J. Knight, L. Divol, E. A. Williams, G. Gregori, B. I. Cohen, C. Constantin, D. H. Froula, D. S. Montgomery, and R. P. Johnson, Phys. Rev. Lett. **93**, 045004 (2004).

29. H. C. Bandulaet *et al.*, Phys. Rev. Lett. **93**, 035002 (2004).

30. B. I. Cohen *et al.*, Phys. Plasmas **12**, 052703 (2005).

31. R. L. Berger *et al.*, Phys. Plasmas **20**, 032107 (2013).

32. E. A. Williams *et al.*, Phys. Plasmas **2**, 129 (1995).

33. T. Chapman *et al.*, Phys. Rev. Lett. **119**, 055002 (2017).

34. R. K. Kirkwood *et al.*, Phys. Rev. Lett. **76**, 2065 (1996).

35. A. Colaïtis, S. Hüller, D. Pesme, G. Duchateau, and V. T. Tikhonchuk, Phys. Plasmas **23**, 032118 (2016).

36. R. K. Kirkwood, D. P. Turnbull, T. Chapman, S. C. Wilks, M. D. Rosen, R. A. London, L. A. Pickworth, W. H. Dunlop, J. D. Moody, D. J. Strozzi, P. A. Michel, L. Divol, O. L. Landen, B. J. MacGowan, B. M. Van Wonterghem, K. B. Fournier, and B. E. Blue, Nat. Phys. **14**, 80 (2018).